SEASAR: HIGH-FIDELITY SIMULATIONS OF MARITIME SAR IMAGES

DJ Pate   Georgia Tech Research Institute, Atlanta, Georgia, USA

1   INTRODUCTION

SeaSAR is a SAR simulation program written in C++ & CUDA for fast computation on a graphics processing unit (GPU). A scene comprising terrain, objects, vehicles, sea surface, etc. is represented by triangulated surfaces, in which the triangles are small enough to capture the physical details that are important to the particular SAR wavelength. The received scattered signal (i.e., the phase history data) is computed by summing over the contributions from every illuminated triangle via physical optics. Because physical optics requires sub-wavelength sampling, X-band radar simulations for appreciable scenes are very computationally intensive, requiring many millions of triangles, depending on scene size and content. SeaSAR features several advanced algorithm and software techniques to quickly and efficiently calculate physical optics scattering on a GPU, such as a bounding volume hierarchy commonly found in computer graphics rendering software. This work focuses on the intersection of physics, signal processing, and GPU programming to allow for efficient high-fidelity SAR simulation over a full scene.

A detailed review of the ship wake SAR simulation literature was recently provided by Rizaev et al.[1], and so only a brief summary is provided here. In general, SAR simulations use the Two-Scale Model (TSM), in which the scattering is divided into two regimes: "the quasi-specular scattering mechanism caused by large-scale gravity waves and the Bragg scattering mechanism caused by small-scale capillary ripples," as described by Linghu et al.[2]. This has also be referred to as a "semi-deterministic" scheme[3]. The sea surface is modeled coarsely, and each surface facet is assigned a scattering strength based on its orientation and the high-frequency portion of the gravity wave spectrum.

Many prior works produce a SAR image directly from the scene by computing a normalized radar cross section (NRCS) for each sea surface facet. Portions of the image are then displaced in the along-track direction according to their radial velocity relative to the sensor to mimic effect that occurs during SAR image formation. This correction is called a "velocity bunching model"[4,5,6]. However, this bypasses the actual signal processing chain and misses the opportunity to model these effects. Alternatively, some authors have developed so-called "SAR raw signal simulators (or generators)" that compute the complex-value time samples for each received pulse[7,8,9,10,11,12,13,14,15]. This form of data is often called the SAR phase history data[16]. Similarly, SeaSAR computes the complex-valued time samples comprising the received signal for every SAR pulse. In this case, along-track displacement due to motion is an *emergent* effect due to directly computing the time of arrival as the scene evolves over time.

The SAR simulation literature remains an active topic of research[17,3,18,19,20,21,22,23,4,24,25].

2   PHYSICAL OPTICS FOR ELECTROMAGNETIC SCATTERING

SeaSAR uses physical optics[26] (PO), also called the Kirchhoff approximation[27,28], in which the surface current at any point is assumed to be equal to the surface current that would be present on a hypothetical infinite tangent plan. Physical optics requires integrating the scattered electromagnetic field over the entire surface with sub-wavelength sampling, except those regions that are shadowed.

The requirement to sample the sea surface with sub-wavelength spacing is extremely burdensome, though that burden is largely alleviated by fast parallel computations with a graphics processing unit (GPU).

Physical optics can be extended to capture multiple scattering, though SeaSAR currently does not include this. Multiple scattering is especially important for capturing dihedrals, which can alter polarization, and trihedrals. The program XPATCH uses the shooting-and-bouncing-rays (SBR) technique as well as the physical theory of diffraction to capture multiple scattering [29,30]. Weinmann extends this to include the propagation of diffracted rays [31]. In general, the multiple scattering problem with physical optics is reminiscent of the global illumination problem in computer graphics [32,33] that is solved via the rendering equation [34]. This suggests the application of modern computer graphics techniques to electromagnetic scattering, which was considered by Willis et al. [35].

Another challenge is properly modeling complex textures beyond that of a polished perfectly electric conducting surface. This is captured in XPATCH via material reflection coefficients [29].

Lastly, regardless of the fidelity of the scattering model, the fidelity of the full simulation can be no better than the representation of the scene, which can often be the limiting factor. Maritime scenes, though, typically comprise only the sea surface, ships, and ship wakes, which is more manageable. SeaSAR includes wind-driven waves [36,37,38,39,40,41,42], Kevlin wakes [43,44,19,22], and turbulent wakes [45,19].

2.1 Scattering Equations

This description of the physical optics scattering equations follows that of Pathak and Burkholder [26,46,47]. The sensor is located at p and the differential scattering element dA of surface S is at q with normal vector $\hat{n}$, and with p and q measured relative to a common origin $\mathcal{O}$, as depicted in Figure 1.
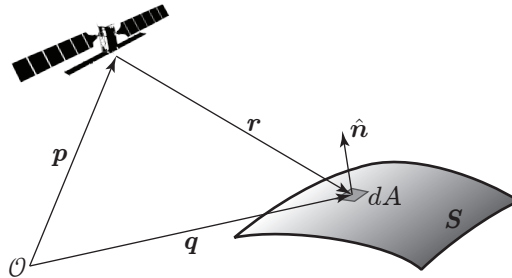

Figure 1: Vector arrangement for the scattering integral.

The relative position vector is $r = q - p$ with length $R = ||r||$ and direction $\hat{r} = r/R$. The incident electric field vector E^i is related to the corresponding magnetic field vector as $H^i = \hat{r} \times E^i / Z_0$, where $Z_0 \approx 376.73$ is the impedance of free space. The incident electric field is determined by the radar aperture, which is currently modeled as a uniform rectangular aperture.

The scattered electric field E^s at q is calculated as

$$E^s(r) = \frac{ik}{4\pi} \int_S \frac{1}{R} \left(\hat{r} \times \hat{r} \times J + \hat{r} \times M \right) \frac{\exp(-ikR)}{R} dA. \tag{1}$$

The physical optics electric and magnetic surface currents are, respectively,

$$J = \hat{n} \times H \tag{2}$$
$$M = E \times \hat{n} \tag{3}$$

and, by the physical optics assumption [47,48,49], the total field is approximated as the sum of the incident

and reflected fields

$$E \approx E^i + E^r \tag{4}$$

$$H \approx H^i + H^r. \tag{5}$$

In the case of a perfect electric conductor, the surface electric current is

$$J = 2n \times H^i \tag{6}$$

while the surface magnetic current is zero[26,50].

2.1.1 Fresnel Reflection Calculation

When the electric field interacts with the sea surface, a Fresnel reflection is applied. The reflected electric and magnetic field vectors are computed via the Fresnel coefficient dyadics

$$E^r = E^i \cdot \underline{\underline{R}}_E \tag{7}$$

$$H^r = H^i \cdot \underline{\underline{R}}_H \tag{8}$$

$$\underline{\underline{R}}_E = \hat{e}^i_\parallel \hat{e}^r_\parallel R_\parallel + \hat{e}_\perp \hat{e}_\perp R_\perp \tag{9}$$

$$\underline{\underline{R}}_H = \hat{e}^i_\parallel \hat{e}^r_\parallel R_\perp + \hat{e}_\perp \hat{e}_\perp R_\parallel. \tag{10}$$

The plane of incidence is spanned by the incident direction $\hat{e}^i = \hat{r}$ and the surface normal vector $\hat{n}$, as seen in Figure 2. Not shown in this diagram is $\hat{e}_\perp$, which is normal to the plane of incidence. Note that superscript i denotes the incident wave and superscript r denotes the reflected wave; the subscript $\parallel$ denotes the parallel polarization direction and subscript $\perp$ denotes the perpendicular polarization direction. The unit vectors $\hat{e}^i$, $\hat{e}^i_\parallel$, and $\hat{e}_\perp$ form an orthonormal basis, as do $\hat{e}^r$, $\hat{e}^r_\parallel$, and $\hat{e}_\perp$.
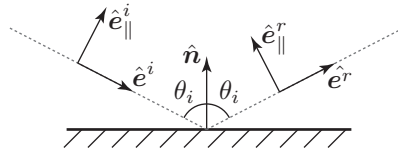

Figure 2: Vector arrangement for Fresnel reflection.

The basis vectors are formed in the following steps:

$$s_\theta = \sin \theta_i = ||\hat{r} \times \hat{n}|| \tag{11}$$

$$c_\theta = \cos \theta_i = -\hat{r} \cdot \hat{n} \tag{12}$$

$$\hat{e}_\perp = \hat{r} \times \hat{n}/s_\theta \tag{13}$$

$$\hat{e}^i_\parallel = \hat{e}_\perp \times \hat{r} \tag{14}$$

$$\hat{e}^r = \hat{r} - 2c_\theta \hat{n}. \tag{15}$$

The angle of incidence θ_i is not actually calculated, since it is not necessary. Instead of doing a vector projection (i.e. Gram-Schmidt processes) to calculate the basis vectors, the cross product for s_θ avoids the cancellation error that is occasionally present, especially with single precision floating-point computations.

Then, with the index of refraction for air n_1 and the index of refraction for seawater n_2, the Fresnel reflection coefficients are calculated as

$$R_\perp = \frac{n_1 c_\theta - n_2 c_t}{n_1 n_2 c_\theta c_t} \tag{16}$$

$$R_\parallel = \frac{n_1 c_t - n_2 c_\theta}{n_1 n_2 c_\theta c_t}. \tag{17}$$

The sign conventions in these calculations are carefully explained by Oh and Vandervelde[51]. The index of refraction of seawater depends both on the physical properties of the water and the electro-magnetic wave frequency[52,53,54].

2.2 Surface Sampling

Physical optics requires solving an integral described in Equation 1 over the surfaces comprising the scene, which in SeaSAR is represented by triangular facets, and so this equation becomes a sum over all the triangles in the scene. Lastly, for each triangle, the surface integral is broken down into a Riemann sum. Therefore, Equation 1 is solved as a very large sampling operation, for which it is important to properly prescribe a sampling grid for each triangle.

The grid for sampling a triangle is constructed by establishing a circumscribed rectangle (that is, a bounding box) and then setting a uniform Cartesian grid inside it. Lastly, only the points on the Carte-sian grid that lie within the triangle are included, as depicted in Figure 3 by the solid blue markers. The grid spacing is typically chosen to be $\lambda/8$.
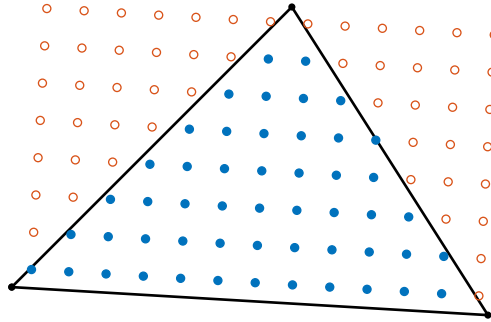

Figure 3: Example sampling grid on a triangle.

2.3 Rectangular Aperture Directivity

In SeaSAR, radar antennas are typically modeled as a uniform rectangular aperture with a spatially-constant current distribution.

The approach to compute the incident electric field vector as explained by Nikolova is built on a set of basis vectors $\hat{\boldsymbol{b}}_1$ (along width), $\hat{\boldsymbol{b}}_2$ (along height), and $\hat{\boldsymbol{b}}_3$ (out toward target), depicted in Figure 4, and spherical coordinates from a traditional physics convention are established with inclination θ and azimuth ϕ[55]. The needed trigonometric terms are computed as

$$\hat{\boldsymbol{\rho}} = \frac{\hat{\boldsymbol{r}} - \hat{\boldsymbol{b}}_3(\hat{\boldsymbol{r}} \cdot \hat{\boldsymbol{b}}_3)}{||\hat{\boldsymbol{r}} - \hat{\boldsymbol{b}}_3(\hat{\boldsymbol{r}} \cdot \hat{\boldsymbol{b}}_3)||} \tag{18}$$

$$c_\theta = \cos\theta = \hat{\boldsymbol{r}} \cdot \hat{\boldsymbol{b}}_3 \tag{19}$$

$$s_\theta = \sin\theta = ||\hat{\boldsymbol{r}} \times \hat{\boldsymbol{b}}_3|| \tag{20}$$

$$c_\phi = \cos\phi = \hat{\boldsymbol{\rho}} \cdot \hat{\boldsymbol{b}}_1 \tag{21}$$

$$s_\phi = \sin\phi = \hat{\boldsymbol{\rho}} \cdot \hat{\boldsymbol{b}}_2 \tag{22}$$

Note that the angles are never actually calculated, and that the the cross product for s_θ is better at avoiding cancellation error than using $\boldsymbol{\rho} \cdot \hat{\boldsymbol{r}}$.
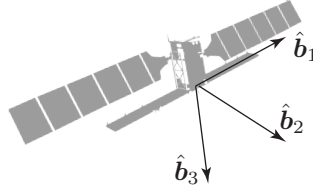
Figure 4: Basis vectors for rectangular aperture.

Next, the azimuth and inclination direction unit vectors are computed as

$$\hat{\boldsymbol{e}}_\theta = c_\theta c_\phi \hat{\boldsymbol{b}}_1 + c_\theta s_\phi \hat{\boldsymbol{b}}_2 - s_\theta \hat{\boldsymbol{b}}_3 \tag{23}$$

$$\hat{\boldsymbol{e}}_\phi = -s_\phi \hat{\boldsymbol{b}}_1 c_\phi \hat{\boldsymbol{b}}_2, \tag{24}$$

which can be derived by differentiating the spherical coordinates.

Finally, the vertically polarized electric field $\boldsymbol{E}^v$ is

$$u = \tfrac{1}{2} k l_x s_\theta c_\phi \tag{25}$$

$$v = \tfrac{1}{2} k l_y s_\theta s_\phi \tag{26}$$

$$C = \tfrac{ik}{4\pi} l_x l_y (1 + c_\theta) \frac{\sin u}{u} \frac{\sin v}{v} \tag{27}$$

$$E_\theta = C s_\phi \tag{28}$$

$$E_\phi = C c_\phi \tag{29}$$

$$\boldsymbol{E}^v = E_\theta \hat{\boldsymbol{e}}_\theta + E_\phi \hat{\boldsymbol{e}}_\phi, \tag{30}$$

where l_x is the array dimension along $\hat{\boldsymbol{b}}_1$, l_y is the array dimension along $\hat{\boldsymbol{b}}_2$, and $i = \sqrt{-1}$. To calculate the horizontal polarization, these same equations are used again but with a swapped l_x & l_y and rotated basis vectors.

Then, as expressed at the beginning of Section 2.1, the incident electric field is the product of $\boldsymbol{E}^v$ and the free-space Green's function $\boldsymbol{E}^i = \boldsymbol{E}^v \exp(-ikR)/R$. Finally, the received scattered electric field is $\boldsymbol{E}^s$ and so the received scattered signal is $z^s = \boldsymbol{E}^v \cdot \boldsymbol{E}^s$ for vertical polarization and likewise for horizontal polarization.

3   SIGNAL PROCESSING

SeaSAR simulates every transmitted, scattered, and received pulse to produce the complex phase history data. This raw data is then pulse compressed via matched filtering[56] and backprojected to form an image[57,58] (backprojection involves delaying and summing according to the round-trip travel time to each pixel.) But, to produce the scattered response for each pulse, the waveform is not computed directly. Rather, the impulse response is computed, instead. Because of the very large number of physical optics computations that are required, it is important to carefully manage the computation of the impulse response.

3.1   Impulse Response

The dependence on time was omitted in previous sections for convenience, but it is needed to express the received signal and its dependence on the transmitted signal. To this end, the incident field is more inclusively written as

$$\boldsymbol{E}^i(\boldsymbol{r}, t) = z^{\text{tx}}(t - \tau) \boldsymbol{E}^v(\hat{\boldsymbol{r}}) \exp(-ikR)/R, \tag{31}$$

for the case of vertical polarization, and $\tau = 2R/c$ is the round-trip travel time. Note that the complex exponential is included to provide the correct phase for every scattering calculation, even though the

transmit signal will be basebanded. This is an expression of *time-domain* physical optics[59,60].

If the transmitted signal needed to be sampled for every calculation involving the incident electric field in the Equation 1, that would greatly compound the computational complexity of the scattering calculation, making it prohibitively expensive. However, with a sufficiently narrow band signal, the scattering can be approximated as frequency independent, and the transmitted signal can be separated from the scattering computation, which instead produces an *impulse response* z^{ir}, as described by Passalacqua et al.[60]. Then, the received signal is the convolution of the transmitted signal and the impulse response

$$z^{\text{rx}} = z^{\text{tx}} * z^{\text{ir}}. \tag{32}$$

Now that the goal is the produce an impulse response, it can be calculated by sampling the surface as

$$z^{\text{ir}}(t) = \sum_k z_k^s \, \text{sinc}(t - \tau_k), \tag{33}$$

where z_k^s is the contribution of the scattered response of the kth sample on the surface S, and τ_k is the corresponding delay. In discretized form, the nth time sample is computed as

$$z_n^{\text{ir}} = z^{\text{ir}}(t_n) = \sum_k z_k^s \, \text{sinc}(t_n - \tau_k), \tag{34}$$

Unfortunately, this is a computational nightmare—there will be *billions* of physical optics samples to compute (index k), and repeating them for every time sample (index n), for which there could be many thousands, should be avoided. The sinc function could be truncated, but it would be far better to completely *decouple* the physical optics calculations from the time series altogether. This is accomplished via *binning*

3.2   Binning

Given a point in a triangle, the time delay will generally not correspond to an exact time in the discretized impulse response signal, and rounding the time to the nearest sample would produce unacceptable phase or timing errors during backprojection. However, if the time sampling grid is refined, then splitting the amplitude of the sample to the two nearest times can produce a sufficient approximation. This is demonstrated in Figure 5—the upper plot presents the underlying sinc that is to be obtained for the example complex amplitude z^s arriving at a particular time. The lower plot demonstrates that two sinc functions, if close enough together, can be summed to accurately approximate this desired result. The purple and green sinc functions are centered on the refined grid, yet they sum together to produce a sinc that is not.

Given a sample rate f_s and time samples t_n with spacing $1/f_s$, consider a refined time sampling grid t_n^r with spacing $1/(f_s/16)$. The superscript $.^r$ here indicates "refined". A refinement factor of sixteen is generally sufficient. Find the nearest time samples that bracket the arrival time τ_k, with $t_{n_a}^r < \tau_k < t_{n_b}^r$. Then calculate corresponding weights w_a and w_b as

$$w_a = (t_{n_b}^r - \tau_k)/(t_{n_b}^r - t_{n_a}^r) = n_b - \tau_k f_s^r \tag{35}$$
$$w_b = (\tau_k - t_{n_a}^r)/(t_{n_b}^r - t_{n_a}^r) = \tau_k f_s^r - n_a. \tag{36}$$

The approximation is established as

$$\text{sinc}(t - \tau) \approx w_a \, \text{sinc}(t - t_{n_a}^r) + w_b \, \text{sinc}(t - t_{n_b}^r), \tag{37}$$

which can then replace the use of $t_n - \tau_k$ in Equation 34. This calculation is analogous to the force carried at the ends of a simply supported beam from a load somewhere in the middle.

Each physical optics sample is contributed to the nearest pairs of sub-samples on the refined grid, and so this is a *binning* operation. The complex amplitudes on the refined sub-sampling grid, t_n^r are
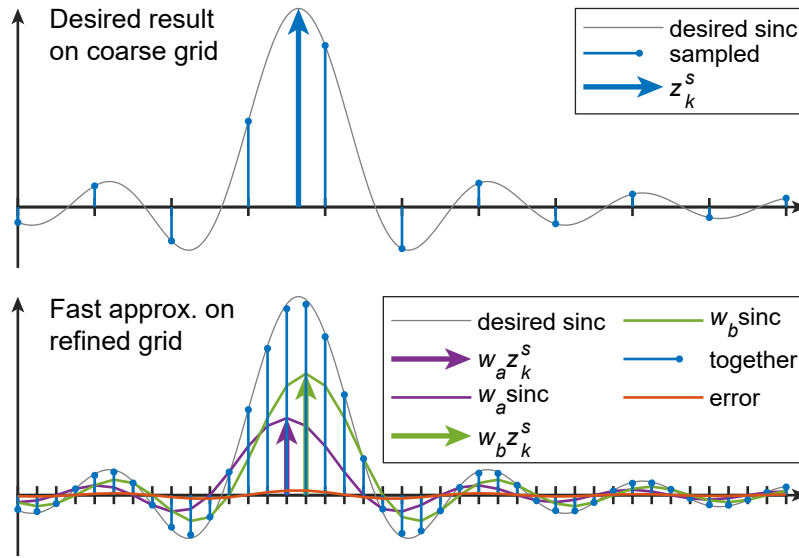
Figure 5: Composing a sinc as the sum of two nearby sincs.

contributed to as

$$z_{n_a}^r \mathrel{+}= w_a z_k^s \tag{38}$$
$$z_{n_b}^r \mathrel{+}= w_b z_k^s \tag{39}$$

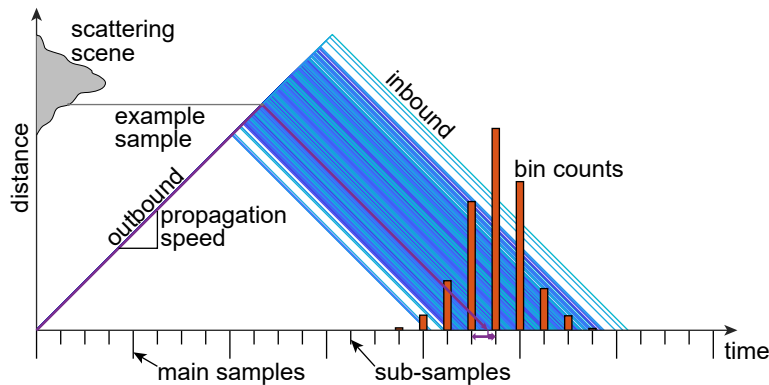for each physical optics sample, and this is demonstrated in Figure 6.

Figure 6: Example binning process.

After all of the physical optics calculations for the entire scene have been completed, the resulting impulse response is calculated as

$$z_n^{\text{ir}} = \sum_m z_m^r \, \text{sinc}(t_n - t_m^r), \tag{40}$$

which has *many* fewer computations than Equation 34.

4   RESULTS

A maritime scene was constructed with an east–west length of 720 meters and a north–south length of 440 m. The SAR platform is 4 km to the west, heading north, and looking back east; the altitude is

3 km. A container ship is placed in the middle heading 30° west of north at 13.5 knots. The resulting SAR image resolution is 0.44 m, and the remaining parameters are provided in Table 1.

First, the scene was held still for the SAR collection, and the resulting image is presented at the top left of Figure 7. The accompanying image in the top right depicts the visual rendering of the scene for context. The brightness of the ship in the SAR image is lower than expected, as seen in an example SAR image in Figure 10. This is likely due to the nature of the 3-D model that was used, in which the 40 ft containers on the ship lack corrugation and other surface features. The flatness of the containers likely acted to favor forward scattering rather than back to the sensor. A more detailed view of the 3-D model is provided in Figure 9. Also, the shadow of the ship is deeper than expected, and this could be due to the lack of noise—no noise was added.

Second, the scene was allowed to progress during the SAR collection, which lasted 0.71 seconds, and the resulting simulated SAR image can be seen at the bottom of Figure 7. Motion toward or away from the sensor causes displacement along-track, which is north–south in this image. Accordingly, the sea surface waves are spread out. Similarly, the ship is displaced northward, which can be observed by comparing it to the optical rendering to the right. Indeed, the image of the ship is on top of its own shadow.

Lastly, a different ship was simulated—a liquefied natural gas (LNG) ship that contains features more amenable to producing a brighter image. The resulting simulated SAR image is provided in Figure 8.

Table 1: Simulation Parameters

platform			sea surface		
altitude	3 km		wind speed	5 m/s	
ground range	4 km		wind fetch	300 km	
speed	250 m/s		wind model	JONSWAP	
heading	north		num. triangles	3,960,000	
looking	east		**container ship**		
radar			length	239 m	
aperture width	0.1 m		beam	33.9 m	
aperture height	0.1 m		draft	10.9 m	
num. pulses	907		speed	13.5 knots	
track length	176.67 m		num. triangles	375,060	
resolution	0.44 m		**LNG ship**		
waveform			length	288.7 m	
center frequency	9.6 GHz		beam	48.1 m	
bandwidth	620 MHz		draft	11.0 m	
pulse duration	1.0 µs		speed	13.5 knots	
sample rate	1.2 GHz		num. triangles	1,876,689	

5   CONCLUSION

SeaSAR is an electromagnetic scattering simulation program based on physical optics calculations performed on a GPU. Also included are signal processing and image processing algorithms, as well as a sea surface and ship wake simulation. The main contribution of this work is *scale*. Taken together, the software, algorithmic, and mathematical approaches combine to enable large-scale physical optics computations. Currently, there are two key features that need to be implemented: textures and multiple scattering.
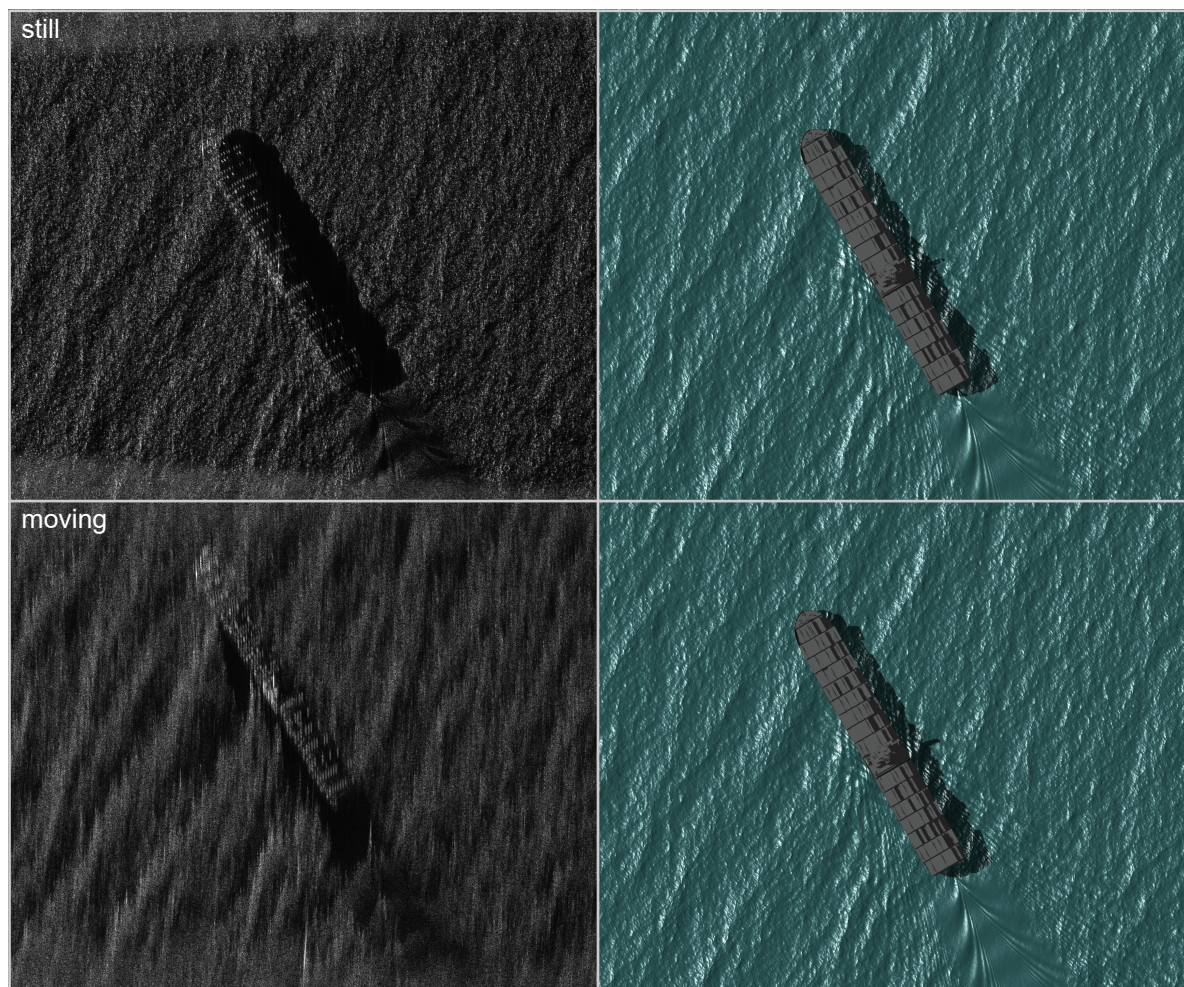
Figure 7: Maersk container ship. (Left) simulated SAR, (right) optical rendering, (top) still scene, (bottom) moving scene. Zoom in to see detail. Ship model attribution: https://skfb.ly/oHQMR
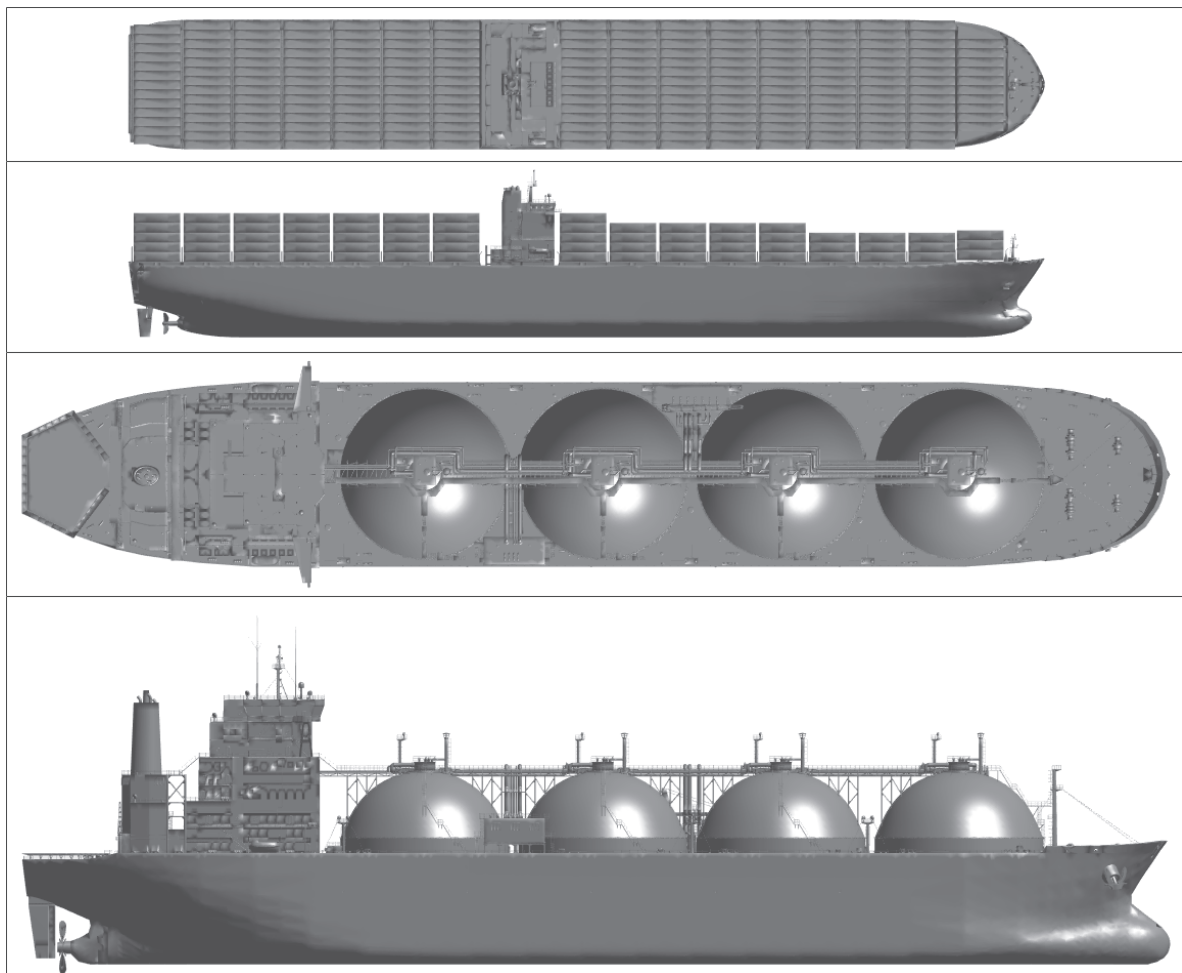

Figure 8: LNG ship in a moving scene. Ship model attribution: https://skfb.ly/6DnWv

Figure 9: (Top) a Maersk container ship (model attribution: https://skfb.ly/oHQMR). (Bottom) an LNG ship (model attribution: https://skfb.ly/6DnWv)
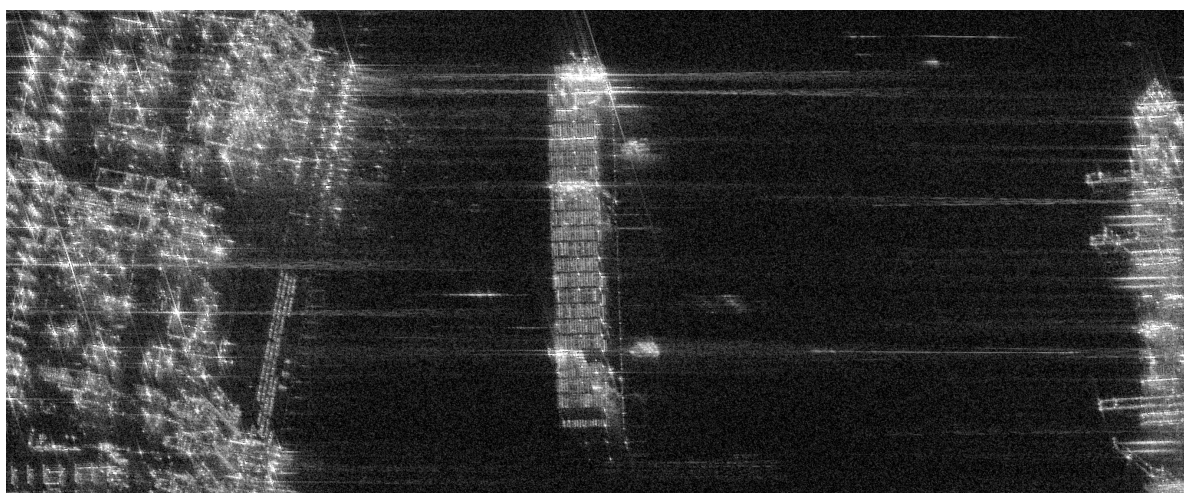

Figure 10: SAR image of a container ship in the Panama Canal. Image credit: Umbra Lab, Inc., 2023

6 REFERENCES

[1] Igor Rizaev, Oktay Karakuş, S John Hogan, and Alin Achim. Modeling and sar imaging of the sea surface: a review of the state-of-the-art with simulations. 2021.

[2] Longxiang Linghu, Jiaji Wu, Zhensen Wu, Gwanggil Jeon, and Xiaobin Wang. Gpu-accelerated computation of time-evolving electromagnetic backscattering field from large dynamic sea surfaces. *IEEE Transactions on Industrial Informatics*, 16(5):3187–3197, 2019.

[3] Hui Chen, Min Zhang, Ding Nie, and Hong-Cheng Yin. Robust semi-deterministic facet model for fast estimation on em scattering from ocean-like surface. *Progress In Electromagnetics Research*, 18:347–363, 2009.

[4] Jia-Kun Wang, Min Zhang, Jun-Long Chen, and Zhaohui Cai. Application of facet scattering model in sar imaging of sea surface waves with kelvin wake. *Progress In Electromagnetics Research*, 67:107–120, 2016.

[5] Jae-Won Rim and Il-Suek Koh. Sar image generation of ocean surface using time-divided velocity bunching model. *Journal of Electromagnetic Engineering and Science*, 19(2):82–88, 2019.

[6] Igor G Rizaev, Oktay Karakuş, S John Hogan, and Alin Achim. Modeling and sar imaging of the sea surface: A review of the state-of-the-art with simulations. *ISPRS Journal of Photogrammetry and Remote Sensing*, 187:120–140, 2022.

[7] Giorgio Franceschetti, Maurizio Migliaccio, Daniele Riccio, and Gilda Schirinzi. Saras: A synthetic aperture radar raw signal simulator. *IEEE Transactions on Geoscience and Remote Sensing*, 30(1):110–123, January 1992.

[8] Giorgio Franceschetti, Antonio Iodice, Maurizio Migliaccio, and Daniele Riccio. Efficient simulation of sar interferometric raw signal pairs. In *IGARSS'97. 1997 IEEE International Geoscience and Remote Sensing Symposium Proceedings. Remote Sensing-A Scientific Vision for Sustainable Development*, volume 4, pages 1701–1703. IEEE, 1997.

[9] Giorgio Franceschetti, Maurizio Migliaccio, and Daniele Riccio. On ocean sar raw signal simulation. *IEEE Transactions on Geoscience and Remote Sensing*, 36(1):84–100, 1998.

[10] Giorgio Franceschetti, Antonio Iodice, Daniele Riccio, Giuseppe Ruello, and Roberta Siviero. Sar raw signal simulation of oil slicks in ocean environments. *IEEE transactions on geoscience and remote sensing*, 40(9):1935–1949, 2002.

[11] Giorgio Franceschetti, Antonio Iodice, Daniele Riccio, and Giuseppe Ruello. Sar raw signal simulation for urban structures. *IEEE Transactions on Geoscience and Remote Sensing*, 41(9):1986–1995, 2003.

[12] Ozan Dogan and Mesut Kartal. Time domain sar raw data simulation of distributed targets. *EURASIP Journal on Advances in Signal Processing*, 2010:1–11, 2010.

[13] Yunkai Deng, Yue Liu, Robert Wang, and Xiaoxue Jia. Fmcw sar raw signal simulator for extended scenes. In *EUSAR 2012; 9th European Conference on Synthetic Aperture Radar*, pages 462–465. VDE, 2012.

[14] Takero Yoshida and Chang-Kyu Rheem. Sar image simulation in the time domain for moving ocean surfaces. *Sensors*, 13(4):4450–4467, 2013.

[15] Weijie Xia, Yuanyuan Qi, Linlin Huang, and Xue Jin. Missile-borne sar raw signal simulation for maneuvering target. *International Journal of Antennas and Propagation*, 2016, 2016.

[16] Robert H Johnston and Wade C Schwartzkopf. Compensated phd–a sensor-independent product for sar phd. In *IGARSS 2019-2019 IEEE International Geoscience and Remote Sensing Symposium*, pages 4519–4522. IEEE, 2019.

[17] James KE Tunaley, Eric H Buller, KH Wu, and Maria T Rey. The simulation of the sar image of a ship wake. *IEEE transactions on geoscience and remote sensing*, 29(1):149–156, 1991.

[18] Min Zhang, Hui Chen, and Hong-Cheng Yin. Facet-based investigation on em scattering from electrically large sea surface with two-scale profiles: Theoretical model. *IEEE Transactions on Geoscience and Remote Sensing*, 49(6):1967–1975, 2011.

[19] Rong-Qing Sun, Gen Luo, Min Zhang, and Chao Wang. Electromagnetic scattering model of the kelvin wake and turbulent wake by a moving ship. *Waves in Random and Complex Media*, 21(3):501–514, 2011.

[20]   Rong-Qing Sun, Min Zhang, Chao Wang, and Yong Chen. Study of electromagnetic scattering from ship wakes on pec sea surfaces by the small-slope approximation theory. *Progress In Electromagnetics Research*, 129:387–404, 2012.

[21]   Qiang Chen. *Convolution quadrature applied to time domain acoustic and electromagnetic scattering problems*. PhD thesis, University of Delaware, 2012.

[22]   Gregory Zilman, Anatoli Zapolski, and Moshe Marom. On detectability of a ship's kelvin wake in simulated sar images of rough sea surface. *IEEE Transactions on Geoscience and Remote Sensing*, 53(2):609–619, 2014.

[23]   Lifan Zhao, Lu Wang, Guoan Bi, and Lei Yang. An autofocus technique for high-resolution inverse synthetic aperture radar imagery. *IEEE Trans. Geoscience and Remote Sensing*, 52(10):6392–6403, 2014.

[24]   Jin-Xing Li, Min Zhang, and Peng-Bo Wei. Effects of breaking waves on composite backscattering from ship-ocean scene. *Chinese Physics Letters*, 34(9):094101, 2017.

[25]   Jinxing Li, Min Zhang, Wenna Fan, and Ding Nie. Facet-based investigation on microwave backscattering from sea surface with breaking waves: Sea spikes and sar imaging. *IEEE Transactions on Geoscience and Remote Sensing*, 55(4):2313–2325, 2017.

[26]   Prabhakar H Pathak and Robert J Burkholder. High-frequency methods. In *Scattering*, pages 245–276. Elsevier, 2002.

[27]   NC Bruce and JC Dainty. Multiple scattering from random rough surfaces using the kirchhoff approximation. *Journal of modern optics*, 38(3):579–590, 1991.

[28]   Feray Hacivelioglu, Levent Sevgi, and Pyotr Ya Ufimtsev. On the modified theory of physical optics. *IEEE transactions on antennas and propagation*, 61(12):6115–6119, 2013.

[29]   Michael Hazlett, Dennis J Andersh, Shung Wu Lee, Hao Ling, and CL Yu. Xpatch: a high-frequency electromagnetic scattering prediction code using shooting and bouncing rays. In *Targets and Backgrounds: Characterization and Representation*, volume 2469, pages 266–275. SPIE, 1995.

[30]   Rajan Bhalla, Luke Lin, and D Andersh. A fast algorithm for 3d sar simulation of target and terrain using xpatch. In *IEEE International Radar Conference, 2005.*, pages 377–382. IEEE, 2005.

[31]   F Weinmann. Utd shooting-and-bouncing extension to a po/ptd ray tracing algorithm. *The Applied Computational Electromagnetics Society Journal (ACES)*, pages 281–293, 2009.

[32]   Per H Christensen, Wojciech Jarosz, et al. The path to path-traced movies. *Foundations and Trends® in Computer Graphics and Vision*, 10(2):103–175, 2016.

[33]   Michal Vlnas. Bidirectional path tracing. In *Proceedings of the 22nd Central European Seminar on Computer Graphics*, volume 1, pages 9–11, 2022.

[34]   James T Kajiya. The rendering equation. In *Proceedings of the 13th annual conference on Computer graphics and interactive techniques*, pages 143–150, 1986.

[35]   Andrew R Willis, Md Sajjad Hossain, and Jamie Godwin. Hardware-accelerated sar simulation with nvidia-rtx technology. In *Algorithms for Synthetic Aperture Radar Imagery XXVII*, volume 11393, pages 108–124. SPIE, 2020.

[36]   Jerry Tessendorf. Simulating ocean water. *Simulating nature: realistic and interactive techniques. SIGGRAPH*, 1(2):5, 2001.

[37]   Jocelyn Fréchot. Realistic simulation of ocean surface using wave spectra. In *Proceedings of the First International Conference on Computer Graphics Theory and Applications (GRAPP 2006)*, pages 76–83, 2006.

[38]   Emmanuelle Darles, Benoît Crespin, Djamchid Ghazanfarpour, and Jean-Christophe Gonzato. A survey of ocean simulation and rendering techniques in computer graphics. In *Computer Graphics Forum*, volume 30, pages 43–60. Wiley Online Library, 2011.

[39]   Per Christensen, Julian Fong, Jonathan Shade, Wayne Wooten, Brenden Schubert, Andrew Kensler, Stephen Friedman, Charlie Kilpatrick, Cliff Ramshaw, Marc Bannister, et al. Renderman: An advanced path-tracing architecture for movie rendering. *ACM Transactions on Graphics (TOG)*, 37(3):1–21, 2018.

[40]   Willard J Pierson and Lionel Moskowitz. A proposed spectral form for fully developed wind seas based on the similarity theory of sa kitaigorodskii. *Journal of geophysical research*, 69(24):5181–5190, 1964.

[41]   Dieter E Hasselmann, M Dunckel, and JA Ewing. Directional wave spectra observed during jonswap 1973. *Journal of physical oceanography*, 10(8):1264–1280, 1980.

[42]   Lining Chen, Yicheng Jin, and Yong Yin. Amplitude malformation in ifft ocean wave rendering under the influence of the fourier coefficient. *Electronics*, 18(2):89–08, 2014.

[43]   Willia Thomson. On ship waves. *Proceedings of the Institution of Mechanical Engineers*, 38(1):409–434, 1887.

[44]   K Oumansour, Y Wang, and J Saillard. Multifrequency sar observation of a ship wake. *IEE Proceedings-Radar, Sonar and Navigation*, 143(4):275–280, 1996.

[45]   JH Milgram, Richard A Skop, Rodney D Peltzer, and Owen M Griffin. Modeling short sea wave energy distributions in the far wakes of ships. *Journal of Geophysical Research: Oceans*, 98(C4):7115–7124, 1993.

[46]   RJ Burkholder. Fast physical optics integration for rough surface scattering. In *IEEE Antennas and Propagation Society International Symposium. Digest. Held in conjunction with: USNC/CNC/URSI North American Radio Sci. Meeting (Cat. No. 03CH37450)*, volume 3, pages 392–395. IEEE, 2003.

[47]   Robert J Burkholder and Teh-Hong Lee. Adaptive sampling for fast physical optics numerical integration. *IEEE transactions on antennas and propagation*, 53(5):1843–1845, 2005.

[48]   K James Sangston. Toward a theory of ultrawideband sea scatter. In *Proceedings of the 1997 IEEE National Radar Conference*, pages 160–165. IEEE, 1997.

[49]   K James Sangston. Analytical aspects of ultrawideband sea scatter. In *Radar Sensor Technology II*, volume 3066, pages 52–63. International Society for Optics and Photonics, 1997.

[50]   Eugene F Knott, John F Schaeffer, and Michael T Tulley. *Radar Cross Section*. SciTech Publishing, 2nd edition, 2004.

[51]   Minsu Oh and Thomas Vandervelde. Bridging the gaps between different sign conventions of fresnel reflection coefficients towards a universal form. In *2020 IEEE 63rd International Midwest Symposium on Circuits and Systems (MWSCAS)*, pages 707–713. IEEE, 2020.

[52]   Kenneth P Hunt, James J Niemeier, and Anton Kruger. Rf communications in underwater wireless sensor networks. In *2010 IEEE International Conference on Electro/Information Technology*, pages 1–6. IEEE, 2010.

[53]   Evangelia A Karagianni. Electromagnetic waves under sea: bow-tie antennas design for wi-fi underwater communications. *Progress In Electromagnetics Research*, 41:189–198, 2015.

[54]   Mark L Mesenbrink. Complex indices of refraction for water and ice from visible to long wavelengths. Technical report, AIR FORCE INST OF TECH WRIGHT-PATTERSON AFB OH, 1996.

[55]   Natalia K. Nikolova. Introduction into the antenna studies. Lecture Notes, 2020.

[56]   Mark A Richards, James A Scheer, William A Holm, Brent Beckley, Principles Mark, A Richards, et al. *Principles of Modern Radar: Basic Principles*. SciTech Publishing, Inc., 2010.

[57]   Michael Israel Duersch. *Backprojection for synthetic aperture radar*. PhD thesis, Brigham Young University, 2013.

[58]   Ali F Yegulalp. Fast backprojection algorithm for synthetic aperture radar. In *Radar Conference, 1999. The Record of the 1999 IEEE*, pages 60–65. IEEE, 1999.

[59]   En-Yuan Sun and WVT Rusch. Time-domain physical-optics. *IEEE Transactions on Antennas and Propagation*, 42(1):9–15, 1994.

[60]   G Passalacqua, M Albani, F Capolino, R Gardelli, M Branciforte, and R Martorana. Algorithm for the estimation of ultrawideband scattering by a target for automotive applications. In *2006 IEEE Antennas and Propagation Society International Symposium*, pages 4391–4394. IEEE, 2006.